Meridional Asymmetry and Energetics of Tropical Instability Waves

ZUOJUN YU,* JULIAN P. MCCREARY JR., AND JEFFREY A. PROEHL**

Nova Southeastern University Oceanographic Center, Dania, Florida

ABSTRACT

One of the striking features of tropical instability waves (TIWs) is that they appear to be more prominent north of the equator. A linearized, $2\frac{1}{2}$-layer ocean model is used to investigate effects of various asymmetric background states on structures of equatorial, unstable waves. Our results suggest that the meridional asymmetry of TIWs is due to asymmetries of the two branches of the South Equatorial Current (SEC) and of the equatorial, sea surface temperature front; it is not due to the presence of the North Equatorial Countercurrent. Energetics analyses indicate that frontal instability associated with the equatorial, SST front, as well as barotropic instability due to shear associated with the SEC, are energy sources for the model TIWs.

1. Introduction

Tropical Instability Waves (TIWs) are a phenomenon common to both the Atlantic and Pacific Oceans (Düing et al. 1975; Legeckis 1977). They are most clearly revealed in satellite sea surface temperature images of the equatorial temperature front ($\sim 3°N$), where they appear as well-organized, cusplike features that propagate westward with periods of 15–45 days and wave lengths of 600–1400 km (Legeckis 1986a,b). The TIWs are an important aspect of equatorial ocean dynamics and thermodynamics, as can be seen in their influence on mean momentum and heat balances. Estimates of the magnitude of Reynolds stresses due to TIWs vary from 0.15 to 0.3 dyn cm^{-2}, a considerable fraction of the local wind stress (~ 0.5 dyn cm^{-2}); estimates of the magnitude of eddy heating vary from 180 to 245 W m^{-2}, values considerably larger than the annual heating rate through the surface (~ 120 W m^{-2}) (Weisberg 1984; Hansen and Paul 1984; Lukas 1987; Weisberg and Weingartner 1988; Bryden and Brady 1989; Luther and Johnson 1990).

One of the striking aspects of TIWs is their *asymmetry* about the equator, particularly with regard to energetics terms. Studies (e.g., Weisberg 1984; Hansen and Paul 1984; Weisberg and Weingartner 1988) have shown that both $\overline{u'v'}\bar{u}_y$ and $\overline{v'T'}\bar{T}_y$ are large and neg-

ative near and north of the equator, suggesting that both barotropic and baroclinic instabilities are energy sources for the TIWs, the former being associated with the shear between the Equatorial Undercurrent (EUC) and the northern branch of the South Equatorial Current (SEC). Most recently, based on data taken during the Tropical Instability Wave Experiment, Qiao and Weisberg (1995) reported that phase lines associated with Pacific TIWs at 140°W tilt against the shear ($\overline{u'v'}\bar{u}_y < 0$) at 1°N and that there is no such tilt at 1°S.

Several studies have also indicated that there may be more than one type of TIW. Based on moored current meter data, Halpern et al. (1988) reported 20-day oscillations in the upper 100–150 m of the eastern Pacific that were largely antisymmetric about the equator with a meridional structure similar to that of a Yanai wave. They also remarked that weaker *lower-frequency oscillations* with periods of 30–50 days were present at depths below 200 m. Using profiling-current-meter data from the Hawaii-to-Tahiti Shuttle Experiment, Luther and Johnson (1990) reported *three distinct* types of instabilities, each occurring at different times of the year. The first occurred during the summer and fall and was due to the strong horizontal shear between the EUC and the northern branch of the SEC. The second occurred in the winter, and its energy source was primarily the mean potential energy associated with the equatorial SST front located from 3°N to 6°N. The third occurred during the spring and utilized the mean potential energy associated with the thermocline tilt beneath the North Equatorial Countercurrent (NECC).

A variety of models, varying in complexity from simple layer models to dynamically sophisticated general circulation models, have been used to study TIWs. Using linearized, $2\frac{1}{2}$- and $1\frac{1}{2}$-layer models,

* Current affiliation: Universities Space Research Association, NASA/Goddard Space Flight Center, Greenbelt, Maryland.
** Current affiliation: Thayer School of Engineering, Dartmouth College, Hanover, New Hampshire.

Corresponding author address: Dr. Zuojun Yu, Mail Code 971, Ocean and Ice Branch, NASA/Goddard Space Flight Center, Greenbelt, MD 20771.
E-mail: yu@toto.gsfc.nasa.gov

Philander (1976) found that when the background state included a representation of a strong SEC and EUC, both centered on the equator, the most unstable wave propagated westward with a period of 16 days and a wavelength of 2000 km. He argued that barotropic instability was the primary energy source for the waves, commenting that baroclinic instability was less likely to be important near the equator where isopycnals associated with geostrophic currents tend to be less sloped. In a second paper, Philander (1978) used only the 1½-layer model (a system in which baroclinic instability is not possible) and adopted a background flow field resembling the northern branch of the SEC and the NECC. The most unstable wave in this case again propagated westward with a period of 30 days and a wavelength of 1100 km. Some subsequent numerical model studies developed instabilities that appeared to result from SEC/NECC shear (e.g., Cox 1980), but others tended to dismiss the role of the NECC in generating TIWs (e.g., Philander et al. 1986), focusing attention on the negative SEC shear just north of the equator.

Motivated to explore the sensitivity of the period of TIWs to the background flow field, Seigel (1985) performed several experiments using Cox's (1980) nonlinear channel model. The background flow consisted of an EUC centered just south of the equator, the northern branch of the SEC, and the NECC. When the maximum speed of the SEC was doubled from 45 cm s^{-1} to 90 cm s^{-1}, the period of TIWs decreased from 30 to 20 days. In a third experiment all the background currents were amplified by 50%, so that the shear between the SEC and EUC was considerably larger than in the other two cases; in this solution, the growth rate for TIWs was smaller and the period was longer than in the test with an increased SEC. Seigel concluded that the period of TIWs was more sensitive to the strength of the SEC itself than to SEC/EUC shear.

A recent study by McCreary and Yu (1992, subsequently referred to as MY92) suggested that the equatorial SST front was important in generating TIWs. Part of their research was carried out using a linearized, 2½-layer system much like Philander's (1976) except that their system allowed temperature variations within layers. This background state was symmetric about the equator and included an EUC, two branches of an SEC, and a cold tongue (see Fig. 1 below). They found two types of unstable waves; both were antisymmetric about the equator and propagated westward. The fastest-growing wave of the first type (Wave 1) was surface trapped with a period of 23.3 days, an e-folding growth scale of 9.1 days, and a wavelength of 785 km. The fastest-growing wave of the second type (Wave 2) was lower layer trapped with a period of 46.9 days, an e-folding growth scale of 14.0 days, and a wavelength of 1571 km. Growth rates for both waves weakened considerably as the upper-layer background temperature
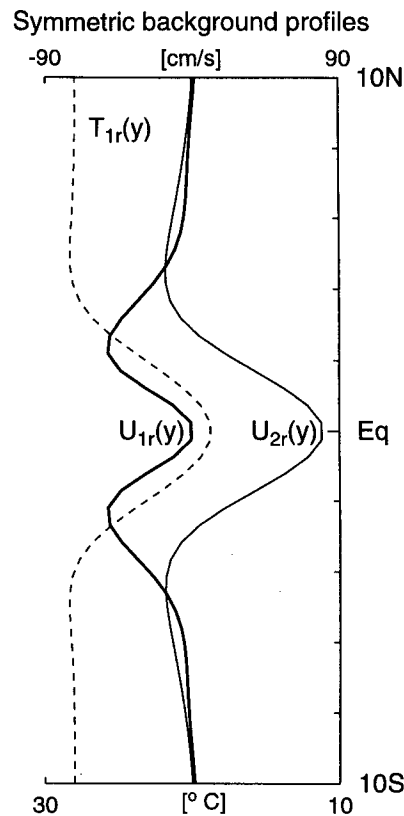

FIG. 1. Profiles of symmetric background flow fields and upper-layer temperature field, U_{ir} and T_{ir}, used in the linear instability model of McCreary and Yu (1992). The lower-layer temperature field T_{2r} is not shown because it is very nearly 15°C everywhere. The prominent features include an eastward EUC, two branches of the westward SEC, and sharp SST fronts on both sides of the equator with T_{ir} being 19°C on the equator.

gradient was reduced, demonstrating that the SST front itself was an important factor in their generation. An energetics analysis showed that the primary energy source of Wave 2 was lower-layer barotropic instability associated with EUC shear. In contrast, a similar analysis revealed that the energy source for Wave 1 was the available potential energy resulting from the variable, upper-layer temperature field, rather than that due to variable layer-thickness fields as in conventional baroclinic instability of the Phillips (1954) sort. [Fukamachi et al. 1995, have recently shown that for mid-latitude fronts this type of instability is closely related to the ageostrophic baroclinic instability studied by Stone (1966, 1970); however, this relationship has not yet been demonstrated for near-equatorial fronts.] The authors referred to this different sort of baroclinic instability as a "frontal instability." Throughout this paper, we also use "frontal instability" to refer to an instability of this type. (Our readers should keep this definition in mind, as other less restrictive meanings are in common use.)

In the same study, McCreary and Yu also identified Waves 1 and 2 to be the initial disturbances in the "main run" of their nonlinear, numerical model, which eventually grew into finite-amplitude, instability waves, labeled f_1 and f_2, respectively (see their Figs. 16a and 16b). Instability f_1 was surface trapped much like the 20-day waves in Halpern et al. (1988), whereas f_2 was intensified in the lower layer similar to the subsurface, lower-frequency variability reported in the same paper. However, neither f_1 nor f_2 exhibited any meridional asymmetries since both the model and the forcing were perfectly symmetric about the equator.

The goal of this research is to determine the dynamical causes for the asymmetry of TIWs and to report on the energetics of asymmetric unstable waves. For this purpose, we use the linearized, $2\frac{1}{2}$-layer model of MY92, which is summarized in section 2. The advantage of linearized models is that it is possible to isolate each unstable wave in the system and so to examine its dynamics in detail. Their major limitation is that the linearized solutions might not correspond well to finite-amplitude disturbances; however, as noted in the previous paragraph, linearized and finite-amplitude solutions do correspond well for the system of interest here. Our approach is to extend the linear instability analysis of MY92 by modifying their background state, so that it is no longer perfectly symmetric about the equator; in particular, we include an asymmetric SEC, a weaker SST front south of the equator, and an NECC. We then discuss how Waves 1 and 2 change in response to these background asymmetries.

2. The ocean model

a. Equations of motion

The ocean model is a linearized, $2\frac{1}{2}$-layer system, consisting of two active upper layers overlying an inert deep region in which the horizontal, pressure-gradient field vanishes. It is obtained by assuming that all variables q in the nonlinear system can be expanded as

$$q = Q(y) + \epsilon q'(x, y, t) + O(\epsilon^2), \quad (1a)$$

where Q is a specified background state independent of x and t, q' is a wave field of the form

$$q' = q^*(\sigma, k, y) \exp(ikx - i\sigma t), \quad (1b)$$

and ϵ is a nondimensional parameter much less than 1. In Eq. (1b), k is the zonal wavenumber and $\sigma(k)$ is a complex frequency with real and imaginary parts, σ_r and σ_i, respectively. With these restrictions, the non-linear equations of motion separate into two linear sets valid at orders 1 and ϵ. We solve the order-ϵ equations for q' fields, obtaining both the dispersion relation $\sigma(k)$ and the structure function $q^*(\sigma, k, y)$ of unstable waves with $\sigma_i > 0$.

With the assumption that the horizontal, pressure gradient field vanishes in the deep ocean, an integration of the hydrostatic relation yields

$$\nabla p_1 = \alpha g \nabla(h_1 \theta_{13} + h_2 \theta_{23}) + \alpha gz \nabla \theta_1, \quad (2)$$
$$\nabla p_2 = \alpha g \nabla[(h_1 + h_2)\theta_{23}] + \alpha gz \nabla \theta_2.$$

In Eqs. (2), p_i, h_i, and θ_i are the pressure, thickness, and temperature of each layer ($i = 1, 2$), respectively; $\theta_{i3} \equiv \theta_i - T_3$, where $T_3 = 0°C$ is the temperature of the quiescent deep ocean, and z represents different depths within each layer. The constant g is the acceleration of gravity, and the coefficient of thermal expansion α has the constant value of $0.00025°C^{-1}$. A factor of ρ_0^{-1} has been absorbed into the definition of pressure here and throughout the paper.

Note that, because the temperature is allowed to vary horizontally within a layer, the pressure gradients vary linearly with depth z. However, such a depth dependence is not possible in a layer model, since each variable in the system is required to remain slablike at all times. Essentially, there is an implicit assumption in the variable-temperature layer model that turbulent stresses exactly balance the depth-dependent parts of ∇p_1 and ∇p_2 in the momentum equations (McCreary and Kundu 1988). It follows that the appropriate pressure gradients for use in the momentum equations are

$$\langle \nabla p_1 \rangle^z = \alpha g \nabla(h_1 \theta_{13} + h_2 \theta_{23}) - \frac{1}{2} \alpha g h_1 \nabla \theta_1,$$
$$(3)$$

$$\langle \nabla p_2 \rangle^z = \alpha g \nabla[(h_1 + h_2)\theta_{23}] - \alpha g \left(h_1 + \frac{1}{2} h_2\right)\nabla \theta_2,$$

the vertical averages of (2) over each layer.

The dynamics of the background state in this model are assumed to be inviscid. Steady, x-independent solutions $Q(y)$ to the resulting order-1 equations are then geostrophically balanced, zonal currents given by

$$U_1 = -(\alpha g/f)\left[(H_1 T_{13} + H_2 T_{23})_y - \frac{1}{2} H_1 T_{1y}\right],$$

$$U_2 = -(\alpha g/f)\left[(H_1 T_{23} + H_2 T_{23})_y \quad (4) \right.$$

$$\left. - \left(H_1 + \frac{1}{2} H_2\right)T_{2y}\right].$$

In Eqs. (4), U_i, H_i, and T_i are the zonal velocity, thickness, and temperature of each layer, respectively, and $T_{i3} \equiv T_i - T_3$. The equatorial β plane is adopted throughout, so that $f = \beta y$.

The order-ϵ equations are

$$u'_{it} + U_i u'_{ix} - (f - U_{iy})v'_i + \langle p'_{ix} \rangle^z = -\nu_4 \nabla^4 u'_i,$$

$$v'_{it} + U_i v'_{ix} + fu'_i + \langle p'_{iy} \rangle^z = -\nu_4 \nabla^4 v'_i,$$

$$h'_{it} + U_i h'_{ix} + H_{iy}v'_i + H_i(u'_{ix} + v'_{iy}) = -\kappa_4 \nabla^4 h'_i,$$

$$\theta'_{it} + U_i \theta'_{ix} + T_{iy}v'_i = -\kappa_4 \nabla^4 \theta'_i,$$
$$(5a)$$

where u_i', v_i', h_i', and θ_i' are the corresponding wave fields for zonal and meridional velocities, layer thickness, and temperature, respectively. The equations also include biharmonic horizontal mixing with coefficients ν_4 and κ_4, both always having the value of 2×10^{21} cm^4 s^{-1} as in MY92. The vertically averaged, pressure gradients in Eq. (5a) are

$$\langle \nabla p_1' \rangle^z = \alpha g \nabla (h_1' T_{13} + h_2' T_{23} + H_1 \theta_1' + H_2 \theta_2')$$
$$- \frac{1}{2} \alpha g (h_1' \nabla T_1 + H_1 \nabla \theta_1'),$$

$$\langle \nabla p_2' \rangle^z = \alpha g \nabla [(h_1' + h_2') T_{23} + (H_1 + H_2) \theta_2']$$
$$- \alpha g \left[\left(h_1' + \frac{1}{2} h_2' \right) \nabla T_2 + \left(H_1 + \frac{1}{2} H_2 \right) \nabla \theta_2' \right], \quad (5b)$$

which are just the order-ϵ terms in the expansion of (3).

Solutions are found in a channel with walls located 15° off the equator. Boundary conditions on the walls are no normal flow and no fluxes through the walls. They are given by

$$v_i' = \theta_{iy}' = h_{iy}' = \nabla^2 v_i' = (\nabla^2 \theta_i')_y = (\nabla^2 h_i')_y = 0, \quad (6)$$

the latter three conditions being required for the biharmonic mixing in the system.

Since q' has the form (1b), the operators ∂_t and ∂_x can be replaced by the complex numbers $-i\sigma$ and ik, respectively. Equations (5) then reduce to a coupled set of differential equations in y alone. They are solved numerically on a linear staggered grid, consisting of segments of width $\Delta y = 0.05°$. The h_i', u_i', and θ_i' points are located at the center of grid segments, and v_i' points are located at their edges. In finite-difference form, the system is a coupled set of algebraic equations, which can be summarized in matrix form. For a given k, the eigenvalues $\sigma(k)$ and eigenfunctions $q^*(\sigma, k, y)$ of the matrix are then determined numerically (Fukamachi 1992). For our solutions, background profiles U_i and T_i are prescribed, and thicknesses H_i are then determined by integrating equations (4) from the southern boundary, where unless specified otherwise a constant value of 75 m is assumed for the thickness.

b. Perturbation energy equation

The perturbation energy equation provides a useful method for analyzing the dynamics of unstable waves (see appendix C of MY92 for its derivation). The equation is

$$\tilde{E}_t = -\tilde{G}_y + \sum_{j=1}^{4} C_j + \mathcal{D}. \quad (7a)$$

The wave energy is defined to be

$$\tilde{E} \equiv \frac{1}{2} H_i \langle u_i'^2 + v_i'^2 \rangle + U_i \langle h_i' u_i' \rangle + \frac{1}{2} \alpha g T_{12} \langle h_1'^2 \rangle$$
$$+ \frac{1}{2} \alpha g T_{23} \langle (h_1' + h_2')^2 \rangle + \alpha g H_1 \langle h_1' \theta_1' + h_2' \theta_2' \rangle$$
$$+ \alpha g H_2 \langle (h_1' + h_2') \theta_2' \rangle, \quad (7b)$$

where $\langle \phi \rangle \equiv 1/\lambda \int_x^{x+\lambda} \phi dx'$ is an average over one zonal wavelength, $\lambda = 2\pi/k$, and summations over repeated layer indices are assumed to hold throughout. [In Eqs. (7) and (9) all primed variables now refer to the real part of the order-ϵ solution; that is, q' has been replaced by the real part of (1b).] The wave energy flux in (7a) is

$$\tilde{G} = \alpha g H_i T_{i3} \langle h_i' v_i' \rangle + \frac{1}{2} \alpha g H_i^2 \langle v_i' \theta_i' \rangle$$
$$+ \alpha g H_1 H_2 \langle v_1' \theta_2' \rangle + \alpha g H_1 T_{23} \langle h_2' v_1' \rangle$$
$$+ \alpha g H_2 T_{23} \langle h_1' v_2' \rangle, \quad (7c)$$

and the interaction terms are

$$C_1 = -(H_i \langle u_i' v_i' \rangle + U_i \langle h_i' v_i' \rangle) U_{iy},$$
$$C_2 = -U_i \langle u_i' \nabla \cdot (H_i v_i') \rangle,$$
$$C_3 = -\alpha g \langle h_1' v_1' \rangle (H_{1y} T_{13} + H_{2y} T_{23})$$
$$- \alpha g \langle h_2' v_2' \rangle (H_{1y} + H_{2y}) T_{23},$$
$$C_4 = -\alpha g \langle h_1' v_1' \rangle (H_1 T_{1y} + H_2 T_{2y})$$
$$- \alpha g \langle h_2' v_2' \rangle (H_1 + H_2) T_{2y}$$
$$- \alpha g H_1 U_1 \left\langle \left(\frac{1}{2} h_1' \right) \theta_{1x}' \right\rangle$$
$$- \alpha g H_2 U_2 \left\langle \left(h_1' + \frac{1}{2} h_2' \right) \theta_{2x}' \right\rangle$$
$$- \alpha g \left\langle \theta_1' \nabla \cdot \left(\frac{1}{2} H_1^2 v_1' \right) \right\rangle$$
$$- \alpha g \left\langle \theta_2' \nabla \cdot \left[H_2 \left(H_1 + \frac{1}{2} H_2 \right) v_2' \right] \right\rangle. \quad (7d)$$

The interaction C_1 is the term that leads to barotropic instability in the upper and lower layers, whereas C_2 is indicative of Kelvin–Helmholtz instability. Term C_3 corresponds to conventional baroclinic instability that taps the available potential energy stored in sloping layer interfaces. Term C_4 causes frontal instability that taps the potential energy associated with the variable temperature fields within each layer (see the introduction). The dissipation term $\mathcal{D}$ includes all expressions involving the mixing coefficients ν_4 and κ_4 (see MY92).

In a physical situation like ours, the traditional procedure for identifying net sources and sinks of wave

energy is to integrate the perturbation energy equation (7a) across the channel to obtain

$$\int \tilde{E}_t \, dy = 2\sigma_i \int \tilde{E} \, dy = \sum_{j=1}^{4} \left(\int C_j \, dy \right) + \int \tilde{D} \, dy. \quad (8)$$

Provided that $\tilde{E}$ is positive definite (and for a growing instability with $\sigma_i > 0$), there is no problem with interpreting (8): a particular energy-conversion term C_j is regarded as being a source of energy for the instability provided that $\int C_j \, dy > 0$, and it is a sink when the sense of the inequality is reversed.

Some of the terms in (7b), however, are not squares of primed quantities, and therefore $\tilde{E}$ is not positive definite. (Non-positive-definite terms arise in layer models because the equation for total energy involves *cubic* expressions, as in the term $1/2 h_i u_i^2$. Thus, in addition to familiar squared terms like $1/2 H_i \langle u_i'^2 \rangle$, the perturbation-energy equation has additional non-positive-definite terms like $U_i \langle h_i' u_i' \rangle$.) One consequence of $\tilde{E}$ not being positive definite is that a *negative* interaction term C_j can now lead to wave growth, provided that regions where C_j and $\tilde{E}$ are both negative tend to overlap; conversely, a *positive* C_j can cause wave decay if regions C_j and $\tilde{E}$, which have opposite signs, overlap. Another consequence is that the energy-flux term $-\tilde{G}_y$ [which integrates out of Eq. (8)] can now also result in wave growth: Suppose that $\tilde{E}$ has both negative and positive values within the channel, say in regions A and B, respectively; in that case, an energy flux from A to B will make $\tilde{E}$ more negative in region A, more positive in region B, and hence will tend to amplify the wave. (Instabilities for which $\int \tilde{E} \, dy$ is identically zero or negative have been discussed in several previous papers: see Cairns 1979; Ripa 1983; Marinone and Ripa 1984; Hayashi and Young 1987; Barth 1989a,b; MY92; Fukamachi et al. 1995.)

To circumvent these conceptual difficulties, we have found that the relation

$$\int \frac{1}{2} (\tilde{E}^2)_t \, dy = 2\sigma_i \int \tilde{E}^2 \, dy = \sum_{j=1}^{4} \left(\int \tilde{E} C_j \, dy \right)$$

$$+ \int \tilde{E}(-\tilde{G}_y) \, dy + \int \tilde{E} \tilde{D} \, dy \quad (9a)$$

provides a useful means for discussing wave energetics; Eq. (9a) follows directly from (7a) after multiplication by $\tilde{E}$. The advantage of (9a) is that its left-hand side is positive definite for a growing instability, and hence it provides an unambiguous measure of wave growth; specifically, any increase (decrease) in the amplitude of the unstable wave, whether it results in more negative or positive energy, will cause an increase (decrease) in $\int \frac{1}{2} \tilde{E}^2 \, dy$. The right-hand side of (9a) states that both interaction C_j and energy flux $-\tilde{G}_y$ terms will tend to amplify the wave (and so can be regarded as being an energy source for the instability) if they are *positively correlated* with $\tilde{E}$. The coefficient,

$$\gamma(q) \equiv \frac{\int \tilde{E} q \, dy}{2\sigma_i \int \tilde{E}^2 \, dy}, \quad (9b)$$

thus provides a nondimensional measure for the strength of a particular energy source term, the sum of all the γ being 1.

As we shall see, for several of our solutions the term $\gamma(-\tilde{G}_y)$ dominates the interaction coefficients $\gamma(C_j)$. How can the nature of the instability be characterized for these solutions? Since $\tilde{G}$ can be an energy source only if $\tilde{E}$ is significantly negative somewhere across the channel, we determine which of the non-positive-definite terms in (7b) causes negative $\tilde{E}$. In each case, we find that $\tilde{E}$ is negative due to the term in (7b) that involves θ_1', and hence we also characterize these solutions as being frontal instabilities.

3. Solutions

For all the solutions, background states consist of a symmetric component that is modified to be asymmetric in a variety of ways. Figure 1 illustrates this symmetric component, showing its current and upper-layer temperature fields (U_{1r}, U_{2r}, and T_{1r}); the lower-layer temperature field (T_{2r}) is not plotted because it is nearly constant with a value of 15°C. The fields are taken from day 90 of the nonlinear, main-run solution of MY92 and averaged to ensure symmetry about the equator (that is, $Q(y) = [q(x_0, y, t_0) + q(x_0, -y, t_0)]/2$, where x_0 is a location near the center of the model ocean basin and t_0 is day 90 of the model integration from a state of rest). Noteworthy features include an eastward EUC, two branches of the westward SEC, and sharp SST fronts on both sides of the equator. The SEC has a maximum westward speed of about 50 cm·s^{-1}, and the EUC reaches 80 cm s^{-1}, both being comparable with observations. The cold tongue is rather intense during the spinup stage, with T_{1r} being 19°C on the equator. When the background state is perfectly symmetric about the equator, solutions exhibit the two prominent antisymmetric unstable waves mentioned in the introduction (Waves 1 and 2 of MY92). In this section, we show how Waves 1 and 2 respond to various asymmetries imposed on this background state.

a. Effect of an asymmetric SEC

For the solutions presented in this subsection, the upper-layer current is given by

$$U_1(y) = \begin{cases} (1 - b_n) U_{1r}(0) + b_n U_{1r}(y), & y > 0 \\ (1 - b_s) U_{1r}(0) + b_s U_{1r}(y), & y \leqslant 0. \end{cases} \quad (10)$$

Fields U_2 and T_i remain unchanged, and the H_i are calculated according to (4). Modification (10) affects the current shear mostly within ±4°, with the southern
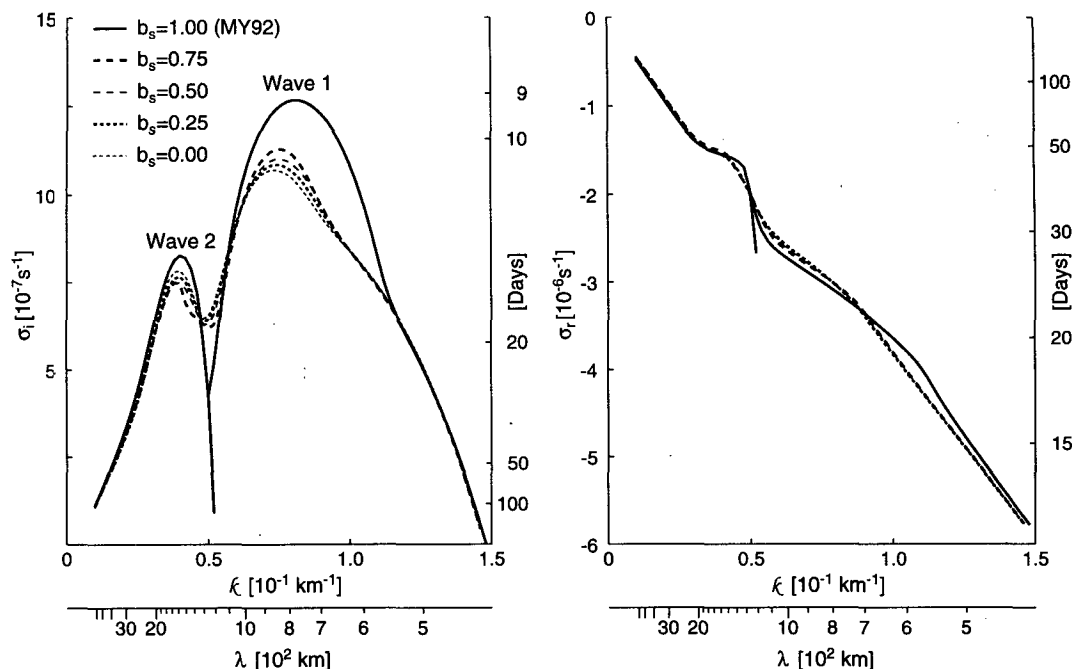
FIG. 2. Imaginary and real parts of the dispersion relation, $\sigma_i(k)$ and $\sigma_r(k)$, for different values of b_s. Waves 1 and 2 correspond to the right-hand and left-hand bands of the $\sigma_i(k)$ curves, respectively. As b_s decreases (that is, as the southern branch SEC weakens), the growth rates for both waves decrease, while the frequencies remain nearly unchanged.

branch of the SEC being weaker than its northern counterpart when $b_n > b_s$. The background state that results when $b_n = 1$ and $b_s = 0.75$ is shown below in the left panel of Fig. 3; in this case, the circulation in the northern ocean is unchanged from that in Fig. 1, but the maximum speed of the southern branch of the SEC is reduced to 38 cm s^{-1}.

Figure 2 shows growth rates σ_i and frequencies σ_r for Waves 1 and 2 when the northern branch of the SEC is unchanged ($b_n = 1$) and the southern SEC is weakened ($b_s < 1$). Figure 3 shows the horizontal structures of the fastest growing waves when $b_s = 0.75$ ($\lambda_1 = 826$ km and $P_1 = 2\pi/\sigma_r = 24.5$ days; $\lambda_2 = 1653$ km and $P_2 = 48.8$ days). As b_s is decreased from 1 to
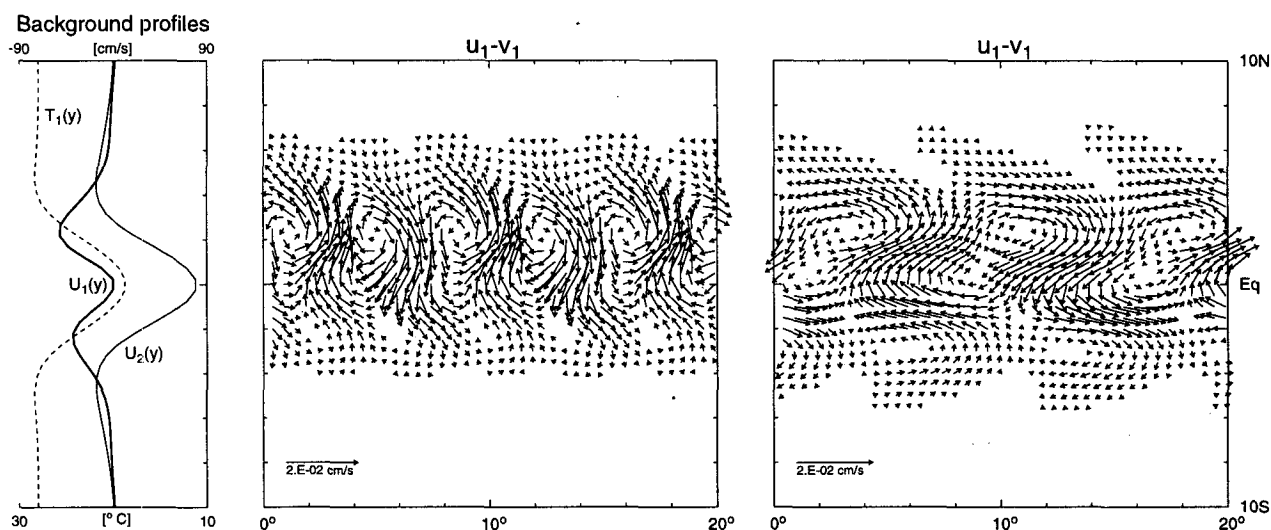

FIG. 3. Structures of upper-layer perturbation velocity fields for Wave 1 (middle panel) and Wave 2 (right panel) with $b_s = 0.75$. Profiles of U_i and T_1 used in this case are provided in the left panel (the profile T_2 is not shown because it is very nearly constant). Although calibration arrows are provided in the lower-left corners of the plots, the magnitudes of the currents are arbitrary. Both waves, especially Wave 1, are much weaker south of the equator, presumably due to the weaker southern branch SEC.

0.75, the frequency σ_r remains nearly unchanged. In contrast, the decrease has a relatively strong influence on the growth rate σ_i and structure of both waves, especially on Wave 1: the two waves now grow more slowly (Fig. 2) and are more concentrated to the north of the equator (Fig. 3). Nevertheless, the perturbation velocities within $\pm 2°$ of the equator remain strong, reminiscent of the findings by Halpern et al. (1988) and by Qiao and Weisberg (1995). With $b_s = 0.5$ (which reduces the maximum speed of the southern SEC to 26 cm s^{-1}) the solutions are even more asymmetric about the equator (not shown), but as b_s is decreased even further they no longer change much (see Fig. 2).

Figure 4a plots profiles of various terms from the energy budget (7) for Wave 1. Note that $\tilde{E}$ is almost everywhere negative (upper panel); indeed, $\int \tilde{E} dy$
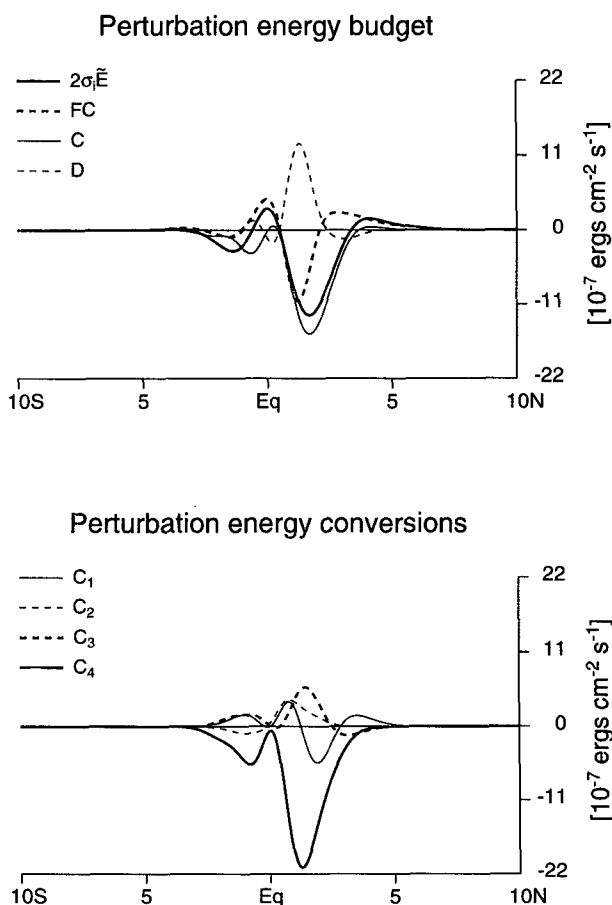
Perturbation energy budget

Perturbation energy conversions

FIG. 4a. Profiles of various terms from the perturbation energy equation for Wave 1 with $b_s = 0.75$. All these quantities are defined precisely in Eqs. (7). The magnitudes of the terms are arbitrary. The upper panel shows plots of $\tilde{E}_t = 2\sigma_i \tilde{E}$, where $\tilde{E}$ is the wave energy, the wave-energy flux convergence (FC), the sum of conversions (C), and the dissipation (D). The lower panel shows the conversion terms, which are indicative of barotropic (C_1), Kelvin–Helmholtz (C_2), baroclinic (C_3), and frontal (C_4) instabilities, respectively. The unstable wave is apparently much less energetic south of the equator due to the weaker C_1 and C_4 terms.
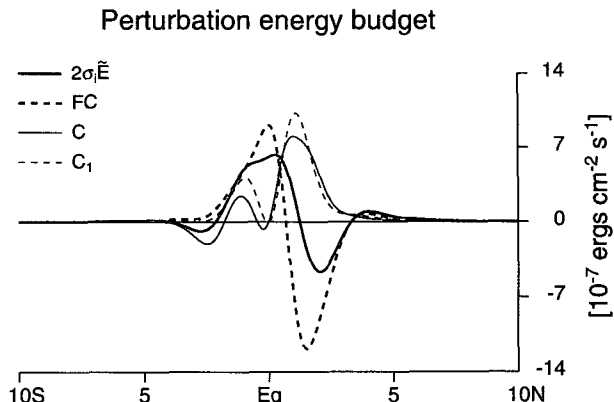
Perturbation energy budget

FIG. 4b. Similar to Fig. 4a except only showing $2\sigma_i \tilde{E}$, FC, C, and C_1 terms for Wave 2 with $b_s = 0.75$. It is shown that the weaker unstable wave south of the equator is mainly due to the weakening of barotropic instability (C_1 term) there.

< 0 so that the wave is an example of a *negative-energy instability*. Both the conversion (C) and wave-energy flux convergence (FC) terms have large amplitudes, and it is obvious that they are both positively correlated with $\tilde{E} [\gamma(C) = 1.14$, and $\gamma(FC) = 0.44]$, implying that they are both energy sources for Wave 1; as expected D is an energy sink for the wave $[\gamma(D) = -0.58]$. To the south, the much reduced amplitude of term C is due to a weakening of both the barotropic and frontal instabilities (C_1 and C_4 in the lower panel). The decrease in C_1 is expected, since it is proportional to the shear associated with the weakened southern SEC. Conversion C_4 is also affected because each term that contributes to it involves either U_i, u'_i, or v'_i, as well as temperature gradient terms [see Eq. (7d)]. The conversion terms are dominated by $C_4 [\gamma(C_4) = 1.42]$, with FC and C_1 being secondary energy sources $[\gamma(FC) = 0.44$, and $\gamma(C_1) = 0.20]$ and the others being sinks $[\gamma(C_2) = -0.15, \gamma(C_3) = -0.33$, and $\gamma(D) = -0.58]$. Since $\gamma(C_4)$ is dominant, we characterize the wave as being a frontal instability.

Figure 4b shows the important terms in the energy budget for Wave 2. In this case, the dominant energy source arises from the FC term $[\gamma(FC) = 1.21]$. This happens because $\gamma(C)$ becomes very small $[\gamma(C) = 0.15]$ due to the development of a significant region of negative $\tilde{E}$ north of the equator, which weakens the correlation. The wave energy $\tilde{E}$ is positive definite without the term in (7b) that involves θ'_1. So, we characterize this wave also to be a frontal instability. [For the symmetric counterpart to the wave ($b_s = 1$), $\gamma(C_1) = 0.74$, $\gamma(FC) = 0.73$, and $\tilde{E}$ is positive almost everywhere (see Fig. 17b of MY92). Thus, this symmetric wave was labeled a barotropic instability in MY92. So, the introduction of asymmetry has considerably altered the energetics of this wave. On the other hand, Wave 2 of MY92 vanished as the SST front was flattened, which implied that the front was essential for its exis-
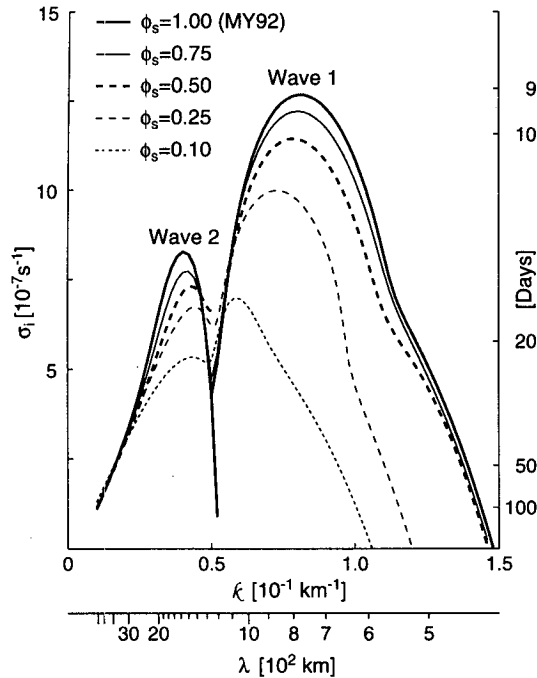
FIG. 5. Similar to Fig. 2 except showing only the imaginary part of the dispersion relation $\sigma_i(k)$ for different values of ϕ_s. As ϕ_s decreases (that is, as the southern SST front weakens), the growth rates for both waves decrease.

tence. In that sense, it should have been labeled a mixed, barotropic frontal instability.]

An asymmetric, unstable wave structure can also be obtained by strengthening the northern branch SEC. For example, the wave structures with $b_n = 1.25$ (corresponding to a maximum westward speed of 60 cm s^{-1}

and $b_s = 1$ are quite similar to those with $b_n = 1$ and $b_s = 0.75$. We conclude that any, relatively small, asymmetry in the SEC can result in TIWs with significant asymmetry.

b. Effect of an asymmetric SST front

The background state for this series of solutions has an asymmetric upper-layer temperature structure given by

$$T_1(y) = \begin{cases} T_{1r}(y), & y > 0 \\ (1 - \phi_s)T_{1r}(0) + \phi_s T_{1r}(y), & y \leqslant 0. \end{cases} \quad (11)$$

The other fields are $U_i = U_{ir}$ and $T_2 = T_{2r}$, and the H_i are calculated from (4). The SST front is weaker south of the equator when $\phi_s < 1$, and the case with $\phi_s = 0.5$ is shown in the left panel of Fig. 6.

Figure 5 gives imaginary parts σ_i of the resulting dispersion curves for Waves 1 and 2 as the meridional SST gradient weakens south of the equator; the real parts σ_r are not shown because they are so similar. Figure 6 shows the horizontal structures of the fastest-growing disturbances ($\lambda_1 = 805$ km and $P_1 = 24.8$ days; $\lambda_2 = 1460$ km and $P_1 = 45.8$ days) when $\phi_s = 0.5$. The change in growth rate σ_i for both waves is substantial as ϕ_s decreases from 1 to 0.25. In contrast, the period of Wave 1 increases by only 1.5 days (from 23.3 to 24.8 days) when ϕ_s decreases from 1 to 0.5, and by another 3.7 days (to 28.5 days) as ϕ_s goes to 0.25; the period of Wave 2 (46.8 days) is nearly unaffected by ϕ_s. The change in the wave structure becomes visually obvious when ϕ_s is 0.5 or less. South of the equator the unstable waves, especially Wave 2, have smaller amplitudes than they do to the north (Fig. 6). Both Waves 1 and 2 are weakened further as ϕ_s reaches
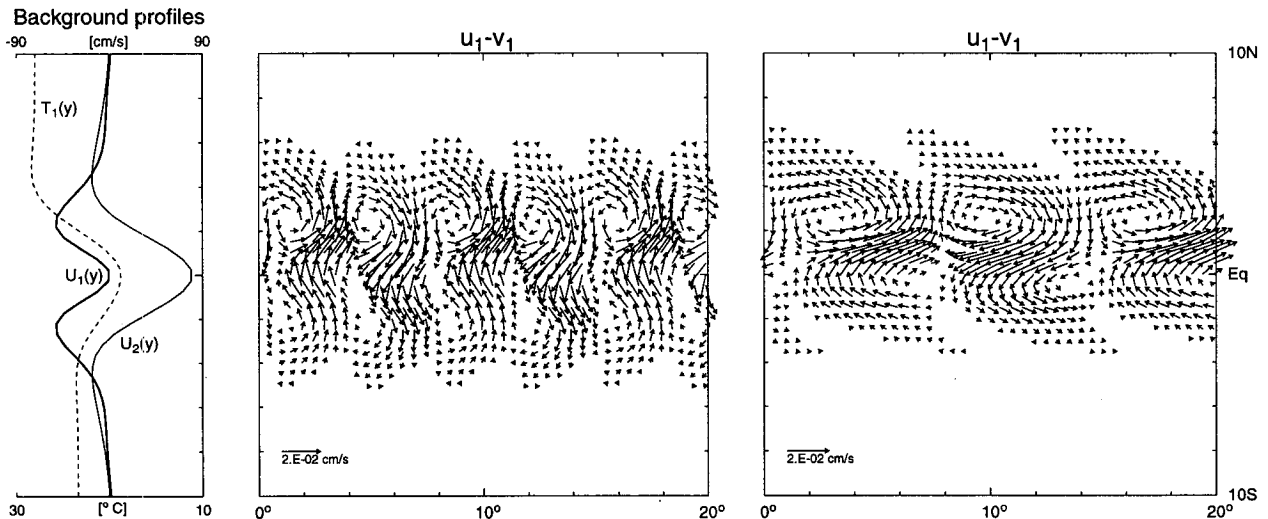

FIG. 6. Similar to Fig. 3 except for $\phi_s = 0.5$. Profiles of U_i and T_1 used in this case are provided in the left panel. Both waves, especially Wave 2, are apparently weaker south of the equator due to the weaker SST front there.

0.1, and it becomes difficult to isolate these waves when ϕ_s is less than 0.075. Therefore, the asymmetry of TIWs may also be caused by the weaker SST front south of the equator.

In the case with ϕ_s = 0.5, $\tilde{E}$ for Waves 1 and 2 is positive definite south of the equator, an indication of the weakening of the frontal instability there; north of the equator, $\tilde{E}$ still has some negative areas (Figs. 7a and 7b). For Wave 1, the impact of the asymmetry is so strong that the FC and C_1 terms become the main energy sources [$\gamma(FC)$ = 0.91, and $\gamma(C_1)$ = 0.49], while the C_4 term contributes only a little [$\gamma(C_4)$ = 0.12]. [The energetics for the symmetric counterpart to this wave with ϕ_s = 1 were dominated by $\gamma(C_4)$; see Fig. 17a of MY92.] Similarly, Wave 2 now gets most of its energy from the C_1 and FC terms [$\gamma(C_1)$ = 0.60, and $\gamma(FC)$ = 0.39]. Again, the regions of negative $\tilde{E}$ are due essentially to the term in (7b) that involves θ'_1. Thus, in this instance (ϕ_s = 0.5) both Waves 1 and 2 appear to be mixed instabilities, with significant contributions from both barotropic and frontal instabilities.

c. Effect of the NECC

For this series, the upper-layer background is modified to include a representation of the NECC according to

$$U_1(y) = U_{1r}(y) + U_{10}\,\mathrm{sech}^2\!\left(\frac{y - Y_0}{L_0}\right)F(y). \quad (12a)$$

The other background fields are $U_2 = U_{2r}$ and $T_i = T_{ir}$; the H_i are calculated according to (4) with $H_1(15°S)$ = 100 m in order to prevent H_1 from becoming negative near the northern wall. In Eq. (12a), U_{10}, Y_0, and L_0 are the amplitude, center location, and width of the NECC. An additional structure function,
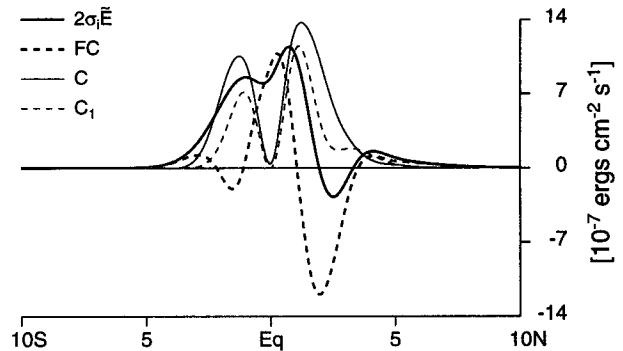
Perturbation energy budget
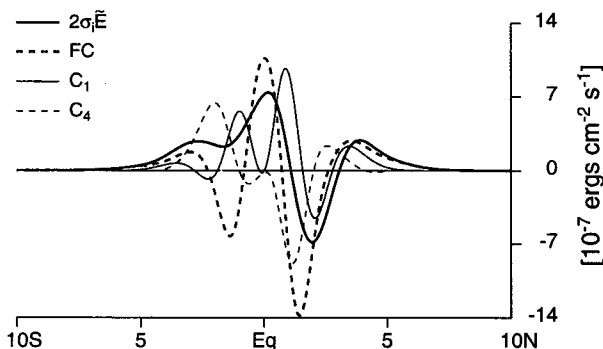

FIG. 7a. Similar to Fig. 4b except showing C_4 term instead of C term, for Wave 1 with ϕ_s = 0.5. Calculations show that $\gamma(FC)$ = 0.91, $\gamma(C_1)$ = 0.49, and $\gamma(C_4)$ = 0.12. Therefore, the wave is a mixed, barotropic-frontal instability, apparently due to the weaker southern SST front.

Perturbation energy budget

FIG. 7b. Similar to Fig. 4b for Wave 2 with ϕ_s = 0.5. The main energy sources in this case are C_1 and FC terms [$\gamma(C_1)$ = 0.60 and $\gamma(FC)$ = 0.39], suggesting that the wave is a mixed, barotropic-frontal instability.

$$F(y) = \begin{cases} 1, & y > Y_0 \\ \dfrac{1}{2} - \dfrac{1}{2}\cos\!\left(\pi\,\dfrac{y - Y_1}{Y_0 - Y_1}\right), & Y_1 \leqslant y \leqslant Y_0 \\ 0, & y < Y_1 \end{cases} \quad (12b)$$

with Y_1 = 3°, is included to cut off the NECC south of 3°N. This cutoff ensures that the maximum speed of the northern SEC, and therefore the shear south of it, is unaffected by the NECC. It is necessary because, as we have demonstrated in section 3a, any relatively small asymmetry in the SEC can cause asymmetric unstable waves.

To simulate the observed NECC, we choose Y_0 = 6°N and L_0 = 2° in Eq. (12a) and vary U_{10} from 0 to 50 cm s^{-1}. The right panel of Fig. 8 shows the imaginary part σ_i of the resulting dispersion curves for Waves 1 and 2. It is clear that the two unstable waves are hardly affected at all by the presence of the NECC, even when U_{10} is increased to 50 cm s^{-1}. The real part of the dispersion relation and the wave structures are not shown because they are virtually unaffected. This insensitivity suggests that the presence of the NECC is not likely to be the cause of the asymmetry of observed TIWs.

4. Summary

The linear instability analysis of MY92 is extended here to investigate the effects of various asymmetric background states on the structures of two types of equatorial unstable waves, namely, Waves 1 and 2 of MY92. These waves are of particular interest because they have properties similar to those for observed TIWs (e.g., Halpern et al. 1988; Qiao and Weisberg 1995). When the background SEC is made asymmetric about the equator with a weaker southern branch, the unstable waves (especially Wave 1) become more prominent
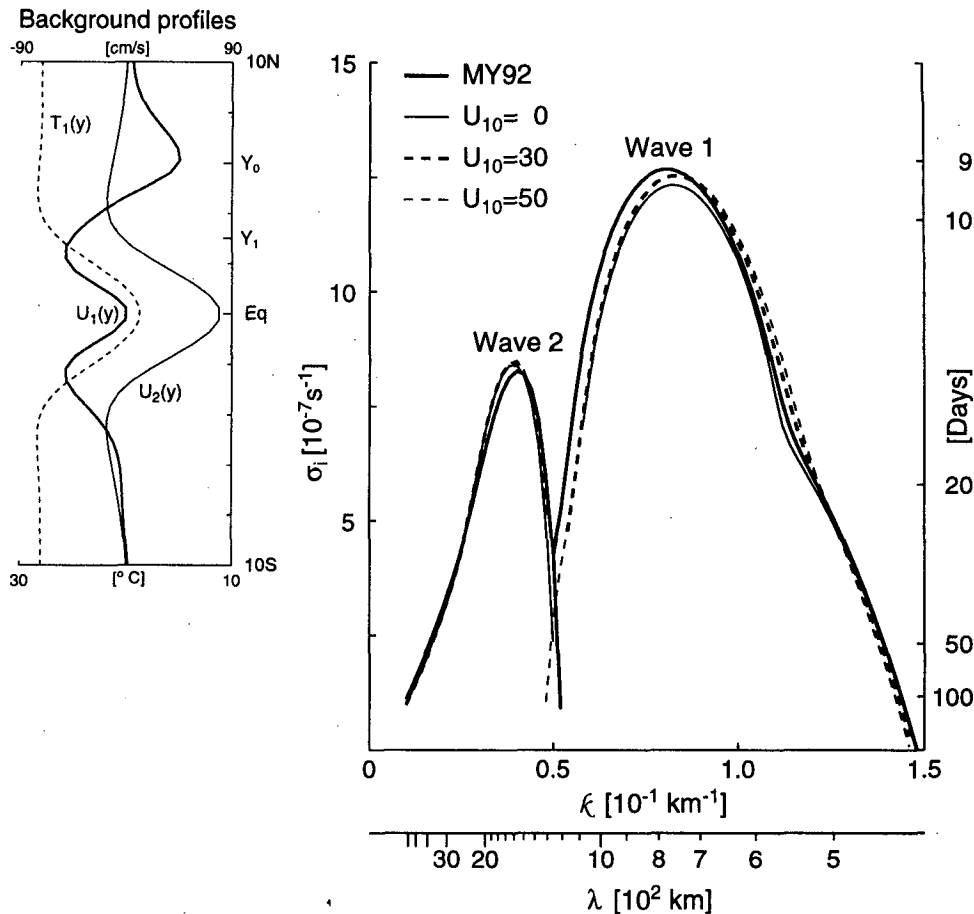
FIG. 8. Similar to Fig. 2 except showing only the imaginary part of the dispersion relation $\sigma_i(k)$ for different values of U_{10}. The profiles of U_i and T_1 are given in the left panel for the case with $U_{10} = 50$ cm s^{-1}. As U_{10} increases from 0 to 50 cm s^{-1}, the growth rates for both waves hardly change at all. [The heavy solid curves in the right panel are for Waves 1 and 2 of MY92, which has $H_1(15°S) = 75$ m.]

north of the equator (Fig. 3). Energetics analyses reveal that the weakening of the unstable waves south of the equator in this case results from weakened barotropic and frontal instabilities there (Figs. 4a and 4b); in addition, they show that frontal instability is the dominant generation mechanism for both waves. When an asymmetric SST front is present, asymmetric unstable waves are again produced (Fig. 6). In this case, due to the weakened SST front south of the equator, the generation mechanism for both waves is mixed, with roughly equal contributions from both barotropic and frontal instabilities. When an idealized NECC is included in the background state, the two waves are hardly affected at all (Fig. 8).

In conclusion, the present study shows that the asymmetry of Waves 1 and 2, and likely the asymmetry of observed TIWs, is due to the meridional asymmetry of the two branches of the SEC and of the equatorial SST front, but not to the presence of the NECC. Additionally, our research (both the present study and MY92) provides theoretical support for the idea of

Luther and Johnson (1990) that there are distinctly different types of TIWs. It should be noted, however, that the existence of two distinct TIWs in our model may be a property specific to a 2½-layer system, which has two active layers and hence two degrees of freedom in the vertical. An alternate explanation for the deeper, lower-frequency variability is that it results from downward propagating free waves generated by a *single*, broadband, instability process confined near the ocean surface (Cox 1980; Philander et al. 1985). There is as yet insufficient data to be able to confirm or reject either hypothesis. Finally, our research indicates that, although barotropic instability due to near-equatorial shear of the SEC does contribute to wave growth, baroclinic instability associated with the strong SST front is the primary energy source for TIWs. Thus, our solutions suggest that the SST front is not simply passively advected by TIWs but rather is an essential part of their dynamics.

REFERENCES

Barth, J. A., 1989a: Stability of a coastal upwelling front, I. Model development and a stability theorem. *J. Geophys. Res.,* **94,** 10 844–10 856.

——, 1989b: Stability of a coastal upwelling front, II. Model results and comparison with observations. *J. Geophys. Res.,* **94,** 10 857–10 883.

Bryden, H., and E. C. Brady, 1989: Eddy momentum and heat fluxes and their effects on the circulation of the equatorial Pacific Ocean. *J. Mar. Res.,* **47,** 55–79.

Cairns, R. A., 1979: The role of negative energy waves in some instabilities of parallel flows. *J. Fluid Mech.,* **92,** 1–14.

Cox, M., 1980: Generation and propagation of 30-day waves in a numerical model of the Pacific. *J. Phys. Oceanogr.,* **10,** 1168–1186.

Düing, W., P. Hisard, E. Katz, J. Knauss, J. Meincke, L. Miller, K. Moroshkin, G. Philander, A. Rybnikov, K. Voigt, and R. Weisberg, 1975: Meanders and long waves in the equatorial Atlantic. *Nature,* **257,** 280–284.

Fukamachi, Y., 1992: Instability of density fronts in layer and continuously stratified models, Ph.D. dissertation, Nova University, 116 pp.

——, J. P. McCreary, and J. A. Proehl, 1995: Instability of density fronts in layer and continuously stratified models. *J. Geophys. Res.,* **100,** 2559–2577.

Halpern, D., R. A. Knox, and D. S. Luther, 1988: Observations of 20-day period meridional current oscillations in the upper ocean along the Pacific equator. *J. Phys. Oceanogr.,* **18,** 1514–1534.

Hansen, D., and C. Paul, 1984: Genesis and effects of long waves in the equatorial Pacific. *J. Geophys. Res.,* **89,** 10 431–10 440.

Hayashi, Y.-Y., and W. R. Young, 1987: Stable and unstable shear modes of rotating parallel flows in shallow water. *J. Fluid Mech.,* **184,** 477–540.

Legeckis, R., 1977: Long waves in the eastern equatorial Pacific Ocean: A view from a geostationary satellite. *Science,* **197,** 1179–1181.

——, 1986a: Long waves in the equatorial Pacific and Atlantic Oceans during 1983. *Ocean–Air Interaction,* **1,** 1–10.

——, 1986b: A satellite time series of sea surface temperatures in the eastern equatorial Pacific Ocean, 1982–1986. *J. Geophys. Res.,* **91,** 12 879–12 886.

Lukas, R., 1987: Horizontal Reynolds stresses in the central equatorial Pacific. *J. Geophys. Res.,* **92,** 9453–9463.

Luther, D. S., and E. Johnson, 1990: Eddy energetics in the upper equatorial Pacific during the Hawaii-to-Tahiti Shuttle Experiment. *J. Phys. Oceanogr.,* **20,** 913–944.

Marinone, S. G., and P. Ripa, 1984: Energetics of the instability of a depth-independent equatorial jet. *Geophys. Astrophys. Fluid Dyn.,* **30,** 105–130.

McCreary, J. P., and P. K. Kundu, 1988: A numerical investigation of the Somali current during the Southwest Monsoon. *J. Mar. Res.,* **46,** 25–58.

——, and Z. Yu, 1992: Equatorial dynamics in a 2½-layer model. Progress in Oceanography, Vol. 29, Pergamon, 61–132.

Philander, S. G. H., 1976: Instabilities of zonal equatorial currents: I. *J. Geophys. Res.,* **81,** 3725–3735.

——, 1978: Instabilities of zonal equatorial currents: II. *J. Geophys. Res.,* **83,** 3679–3682.

——, D. Halpern, D. Hansen, D. Legeckis, R. Miller, C. Paul, R. Watts, R. Weisberg, and M. Wimbush, 1985: Long waves in the equatorial Pacific Ocean. *Trans. Amer. Geophys. Union,* **66,** 154–155.

——, W. J. Hurlin, and R. C. Pacanowski, 1986: Properties of long equatorial waves in models of the seasonal cycle in the tropic Atlantic and Pacific oceans. *J. Geophys. Res.,* **91,** 14 207–14 211.

Phillips, N., 1954: Energy transformations and meridional circulations associated with single baroclinic waves in a two-layer model. *Tellus,* **6,** 273–280.

Qiao, L., and R. H. Weisberg, 1995: Tropical instability wave kinematics: Observations from the Tropical Instability Wave Experiment (TIWE). *J. Geophys. Res.,* in press.

Ripa, P., 1983: General stability conditions from zonal flows in a one-layer model on the β-plane or the sphere. *J. Fluid Mech.,* **126,** 463–487.

Seigel, A. D., 1985: A comment on long waves in the Pacific Ocean. *J. Phys. Oceanogr.,* **15,** 1881–1883.

Stone, P. H., 1966: On non-geostrophic baroclinic stability. *J. Atmos. Sci.,* **23,** 390–400.

——, 1970: On non-geostrophic baroclinic stability: Part II. *J. Atmos. Sci.,* **27,** 721–726.

Weisberg, R. H., 1984: Instability waves observed on the equator in the Atlantic Ocean during 1983. *Geophys. Res. Lett.,* **11,** 753–756.

——, and T. J. Weingartner, 1988: Instability waves in the equatorial Atlantic Ocean. *J. Phys. Oceanogr.,* **18,** 1641–1657.